Journal of Power Sources 196 (2011) 2640–2643

Contents lists available at ScienceDirect

Journal of Power Sources

journal homepage: www.elsevier.com/locate/jpowsour

Short communication

Impact of pore microstructure evolution on polarization resistance of Ni-Yttria-stabilized zirconia fuel cell anodes

J. Scott Cronin, James R. Wilson, Scott A. Barnett*

Department of Materials Science and Engineering, Northwestern University, 2220 Campus Dr., Evanston, IL 60208, USA

ARTICLE INFO

Article history:
Received 13 October 2010
Accepted 22 October 2010
Available online 3 November 2010

Keywords:
SOFC
3D
Microstructure
FIB-SEM
Degradation
Ni-YSZ

ABSTRACT

Temperature induced degradation in Solid Oxide Fuel Cell (SOFC) Ni-YSZ anodes was studied using both impedance spectroscopy and three-dimensional tomography via Focused Ion Beam–Scanning Electron Microscopy. A 100 h anneal at 1100 °C caused a 90% increase in cell polarization resistance, which correlated with the observed factor of ~2 reduction in the electrochemically active three-phase boundary (TPB) density. The TPB decrease was caused by a significant decrease in pore percolation, and a reduction in pore interfacial area due to pores becoming larger and more equiaxed. The anneal caused no measurable change in average Ni particle size; Ni coarsening was apparently highly constrained in these anodes due to the relatively large YSZ volume fraction and low pore volume.

1. Introduction

Long-term (>40,000 h) stability is an important requirement for the commercial viability of SOFCs for stationary power applications. Many stability studies have focused on extrinsic degradation effects due to impurities in the fuel [1,2], in stack components such as interconnects and seals [3,4], or in the SOFC materials themselves [5,6]. On the other hand, studies of degradation mechanisms that are intrinsic to the SOFC materials – e.g., cation diffusion [7], steam–anode interactions [8,9], and electrode sintering/coarsening [10,11] – can help determine "fundamental" limits on stability. Prior work has often focused on microstructural evolution of Ni–Y_2O_3 stabilized ZrO_2 (YSZ) SOFC anodes, suspected to be a major cause of long-term SOFC performance loss. High-temperature (>800 °C) annealing of these anodes has been shown to cause an increase in average Ni particle size and a decrease in TPB density [12–14]. However, the measurements were made using stereological analysis of 2D microscopy images, which does not provide information on three-dimensional structural parameters – e.g., phase connectivity and tortuosity – that have been shown to impact electrode performance [15]. Other studies have quantified Ni-YSZ electrochemical degradation during prolonged life tests [16,17]. A more complete understanding of anode degradation will likely require studies that directly correlate detailed microstructural data with changes in electrochemical response.

Recent advancements in Focused Ion Beam—Scanning Electron Microscopy (FIB-SEM) tomography allow quantitative three-dimensional characterization of electrode microstructure [15,18–23]. This method yields accurate interfacial area and TPB density values [19] as well as phase connectivity and tortuosity information. It thus provides a new opportunity for complete and quantitative observations of the microstructural evolution of Ni-YSZ anodes such that more direct correlation with electrochemical performance loss can be made. In addition, 3D data sets can also be used as experimental inputs for modeling groups in order to extrapolate performance loss over much longer timescales [19,24].

This letter describes initial experiments where Ni-YSZ anode-supported cells were annealed without any current at elevated temperature (1100 °C) in order to accelerate structural changes that normally occur over much longer times, as is similar in prior studies [12,16]. A novel method was used to add infiltrated cathodes to the cells after annealing, making it easier to isolate anode performance changes observed in electrochemical impedance spectroscopy (EIS) measurements. FIB-SEM tomography was used to observe microstructural changes in the anode functional layers caused by annealing, and the results were correlated with the measured anode performance changes.

2. Experimental

The Ni-YSZ anode samples were processed using methods similar to anode-supported cells [25]. 50:50 wt% NiO:YSZ functional layers and YSZ electrolyte layers were deposited from colloidal solutions on dry-pressed 50:50 wt% NiO (J.T. Baker):YSZ (Tosoh)

* Corresponding author. Tel.: +1 847 491 2447; fax: +1 847 491 7820.
E-mail address: s-barnett@northwestern.edu (S.A. Barnett).

0378-7753/$ – see front matter © 2010 Elsevier B.V. All rights reserved.
doi:10.1016/j.jpowsour.2010.10.084

supports, and the structures were co-sintered at 1400 °C for 4 h. Another YSZ layer was then deposited by screen printing and fired at 1200 °C for 2 h to produce a porous scaffold for cathode impregnation.

Some of the samples were annealed for 100 h in a 4% H_2–3% H_2O–93% Ar mixture at 1100 °C, while non-annealed samples served as a baseline for comparison. This gas composition was chosen to replicate conditions experienced during fuel cell operation while maintaining a safe experimental design. The porous YSZ scaffolds of all cells were then infiltrated with a solution containing samarium, strontium, and cobalt nitrates, using a procedure previously shown to produce low-resistance $Sm_{0.5}Sr_{0.5}CoO_{3-\delta}$ (SSC) cathodes [26]. The cells were then sealed to alumina tubes and heated to 800 °C with H_2 fuel supplied to the anode and air to the cathode. The cells were maintained at 800 °C for ~1 h, sufficient to form the SSC perovskite phase in the cathode [26], prior to electrochemical testing. Adding the infiltrated cathode after anode annealing assured that the cathodes were similar regardless of the annealing condition. Electrochemical impedance spectroscopy (EIS) measurements were collected using a Zahner IM6 electrochemical testing station.

The cells were then fractured and vacuum-infiltrated with a low viscosity epoxy (Buehler) [27], and serial-sectioned using a Zeiss Nvision 40 dual beam FIB-SEM system with a 2 kV electron beam energy and in-lens detector. Image resolution was 25 nm in the SEM images and the spacing between images was 50 nm. 3D image reconstruction was carried out as described elsewhere [28]. Two approximately cubic-shaped reconstructions were obtained with volumes of 914 (non-annealed) and 1121 μm^3 (annealed). These volumes were large enough to provide good statistics and, combined with the resolution noted above, allowed calculations of interfacial areas and TPB lengths with errors of ~5% [29,30].

The network connectivity of each phase was analyzed using a directional method: YSZ was considered connected if it extended from the electrolyte, while Ni and pore phases were required to extend from the support layer [31]. TPB density [15,28] and pore tortuosity [18] were calculated as described previously.

3. Results and discussion

3.1. Electrochemical impedance spectroscopy analysis

Fig. 1 shows Nyquist (a) and Bode (b) plots comparing the EIS data from the non-annealed and 1100 °C annealed cells. The total cell polarization resistance of the annealed sample was 0.75 Ω cm^2, ~90% larger than the value for the non-annealed cell, 0.39 Ω cm^2. A number of observations indicated that this change was related to the anode. First, separate measurements of the infiltrated cathodes in symmetric cells (prepared identically to the procedure described above, but on dense YSZ pellets) showed that the cathode polarization resistance was only 0.04 Ω cm^2, a small fraction of the total polarization. Second, Fig. 1(b) shows that the difference in impedance response between the non-annealed and annealed cell was observed in the 0.1–10^3 Hz range, whereas the main response of the cathode in the symmetric cells was at 10^4 Hz. Third, when the anode was supplied with a 50 mol% H_2–50 mol% Ar mixture instead of pure H_2, as shown in Fig. 1(b), the same 0.1–10^3 Hz responses increased. Fourth, prior EIS studies of Ni-YSZ anode supported cells have shown responses sensitive to fuel composition similar to the present data, in the 1–10^4 Hz range [32,33].

3.2. 3D microstructural analysis

Fig. 2 shows typical 2D FIB-SEM images from the non-annealed (a) and annealed (b) cells. Although both showed good contrast between the Ni (white), YSZ (gray), and epoxy-filled pore phases (black), the annealed anode had a significant fraction of pores that did not fill with epoxy. Fig. 2(c) and (d) shows the corresponding 3D reconstructed images of the anode functional layers.

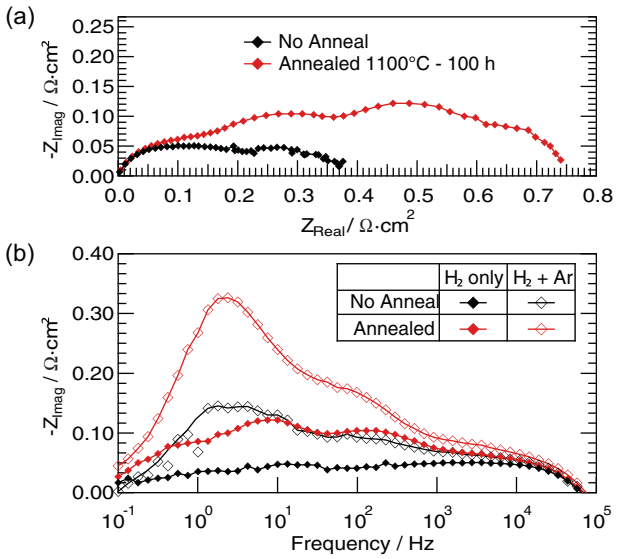

Fig. 1. (a) Nyquist plot of impedance data, measured in dry hydrogen, comparing cells with non-annealed and annealed anodes. The high frequency real-axis intercepts were set to zero to provide a direct comparison of the polarization arcs. (b) Bode plots of the data shown in (a), along with data taken from the same cells in dry 50% H_2–50% Ar mixtures.

Structural information obtained from the reconstructions is shown in Table 1. The volume percentages of the phases agreed, within experimental error, with the predicted values – 27.6% Ni, 53.1% YSZ, and 19.3% pore – based on the initial weight ratio of NiO and YSZ and assuming that the as-fired NiO-YSZ active layer was 100% dense prior to Ni reduction. The agreement of the annealed and non-annealed samples shows that there was no net change in anode composition (e.g., due to evaporation [17]) during annealing.

There was a 25% reduction of the pore specific interfacial area (pore interfacial area normalized by pore volume) as shown in Table 1, indicating that the pores became larger and/or more equiaxed. The reduced pore specific area likely results from Ni mobility combined with limited YSZ mobility; higher Ni mobility is expected since the 1100 °C annealing temperature was 80% of the Ni melting point versus only 45% of the YSZ melting point. Note that limited YSZ mobility was indicated by the ~7% decrease in YSZ specific interfacial area (Table 1). The Ni specific interfacial area

Table 1
Calculations on 3D structural data collected by FIB-SEM tomography.

	Non-annealed	Annealed	% Change
Vol% Ni	27.8	26.5	
Vol% YSZ	54.1	53.8	
Vol% pore	18.1	19.7	
Specific Ni interfacial area (μm^{-1})	5.66	5.76	+1.70
Specific YSZ interfacial area (μm^{-1})	4.83	4.51	−6.59
Specific pore interfacial area (μm^{-1})	9.76	7.30	−25.2
Ni-pore intefacial area (μm^{-1})	0.36	0.27	−26.1
YSZ-pore interfacial area (μm^{-1})	1.40	1.17	−16.6
Ni-YSZ interfacial area (μm^{-1})	1.21	1.26	+3.87
TPB density (μm^{-2})	3.37	2.50	−25.9
Active TPB density (μm^{-2})	2.60	0.74	
Unknown TPB density (μm^{-2})	0.34	1.18	
Inactive TPB density (μm^{-2})	0.43	0.58	
Tortuosity	5.51	6.06	+10.0

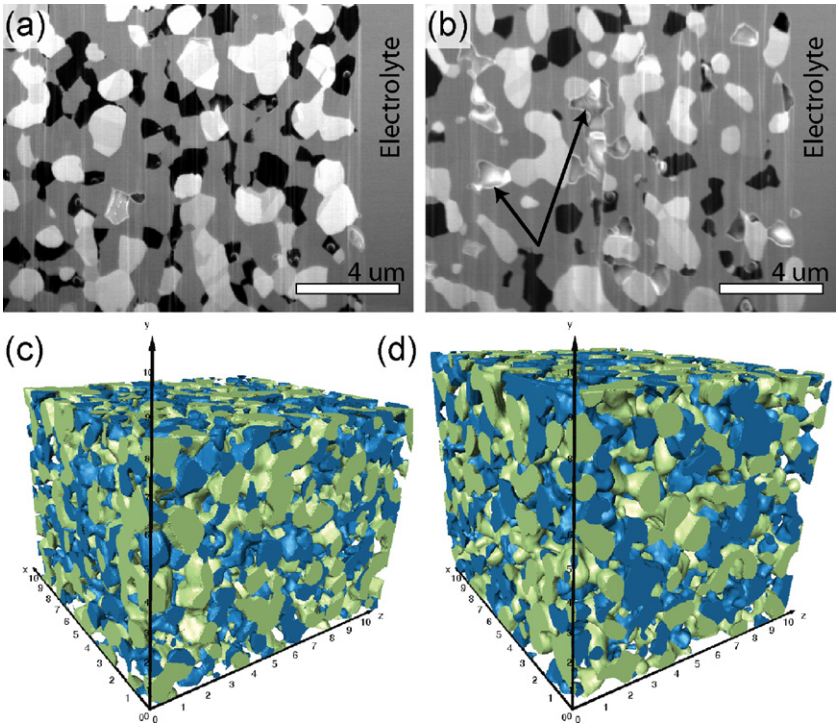

Fig. 2. 2D micrographs of the non-annealed (a) and annealed (b) anode functional layers used to make the reconstruction. Two of the pores that did not fill with epoxy are indicated with arrows in (b). The corresponding 3D image reconstructions are shown in (c) and (d), with Ni appearing as green, pore as blue, and YSZ transparent. (For interpretation of the references to color in this figure legend, the reader is referred to the web version of the article.)

remained approximately constant, a surprising result given prior reports. However, of the total Ni interfacial area, 80% is between Ni and YSZ. Thus, even though Ni-pore interfacial area decreased by 28%, it did not have much effect on the overall Ni particle size. That is, Ni attempted to coarsen at the Ni-pore interface, while the more prevalent YSZ phase strongly constrained the overall change in the average Ni particle size.

The total TPB length decreased 26%, from 3.37 μm^{-2} for the non-annealed anode to 2.50 um^{-2} for the annealed anode. This can most likely be explained by the above-noted reduction of interfacial areas resulting in formation of fewer TPBs. However, total TPB density is not the whole story, as TPBs must lie on fully percolated phases in order for electrochemical reactions to occur. In both samples, YSZ was fully percolated, not surprising given its 53% volume fraction. The Ni phase in the non-annealed anode was 1.8 vol% isolated and 3.3 vol% unknown, and these values were slightly higher – 4.2 vol% isolated and 4.4 vol% unknown – in the annealed sample. The "unknown" portion corresponds to particles that appear isolated but intersect the boundary of the FIB-SEM measured volume, such that their percolation cannot be determined [15]. The pore volume was 2% isolated and 5% unknown without annealing, and increased to 7% isolated and 52% unknown for the annealed anode. Fig. 3 depicts 3D reconstructions of the anode pore phase showing the active, unknown, and isolated portions. Note that most

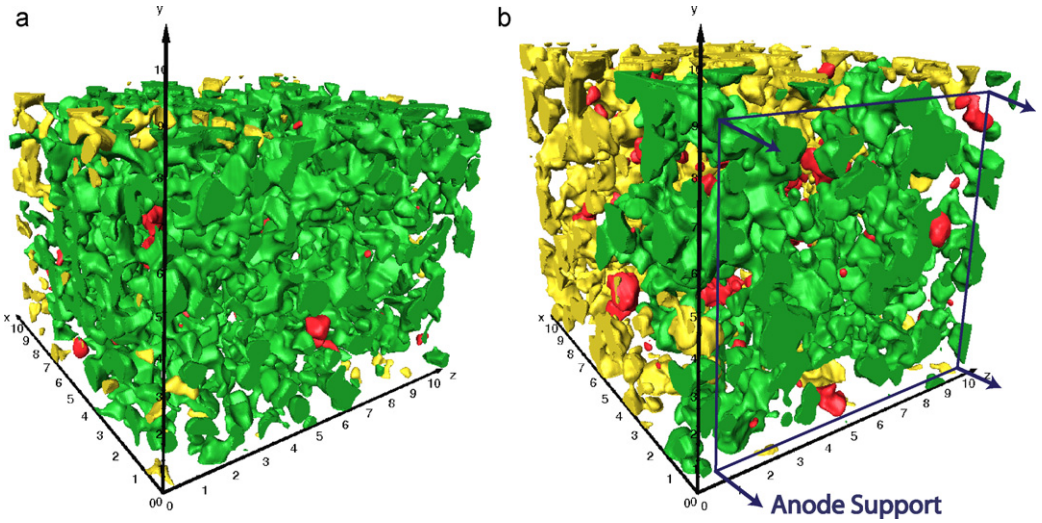

Fig. 3. 3D image reconstructions showing the connectivity of the pore phase of the non-annealed (a) and annealed (b) anode functional layers. Red represents isolated pores, yellow represents pores of unknown status, and green represents pores that are connected to the front-right face of the image, which is the side contacting the current collector and fuel supply as indicated in (b). (For interpretation of the references to color in this figure legend, the reader is referred to the web version of the article.)

of the isolated and unknown pores were towards the back of the image, as expected since these pores were furthest from the Ni-YSZ support (and hence to the fuel gas supply) at the front side of the image. The actual fraction of isolated pores can be estimated by assuming that unknowns have the same fraction isolated as the overall population. This approach results in ~2% isolated pores in the non-annealed anode, and ~15% isolated pores in the annealed anode. Note that the substantial fraction of isolated pores explains the observation of poor epoxy infiltration of the annealed anode, noted previously in Fig. 2(b).

The electrochemically-active TPB (EA-TPB) density was determined by including only TPBs that were on percolated pores and Ni. For the non-annealed anode, the EA-TPB density was ~2.9 μm^{-2}, while the annealed anode had a value of ~1.4 μm^{-2}. The decrease in EA-TPB density is reasonably consistent with the increase in anode polarization resistance, from ~0.39 to ~0.75 $\Omega\,cm^2$ (Fig. 1). The EIS data may also include a component of concentration polarization that would be affected by changes in pore structure, particularly the tortuosity and volume fraction of percolated porosity. Tortuosity values obtained from the 3D data increased slightly from 5.5 for the non-annealed to 6.1 for the annealed anode, while the percolated pore volume decreased by ~15%. These changes likely account for part of the polarization resistance increase due to annealing.

4. Summary and conclusions

FIB-SEM 3D tomography studies showed that high temperature annealing of Ni-YSZ anode functional layers resulted in a factor of ~2 reduction in the electrochemically-active TPB density. This decrease was consistent with the observed increase in anode polarization resistance. The active TPB density reduction resulted from two main structural changes: (1) a decrease in total TPB density associated with a decrease in pore interfacial area, and (2) a decrease in pore percolation that increased the population of inactive TPBs. The latter effect, which was the most significant structural change observed, has not been reported previously. The present results are characteristic of low porosity, low Ni content anodes made using high sintering temperature with no pore formers; in this case the high YSZ volume fraction limited changes in Ni particle size, but the low pore volume probably maximized the tendency for pores to become isolated. Different anode compositions, particle sizes, and pore volumes may yield different anode structure changes. Anodes made with added pore formers, higher Ni content, and/or lower anode firing temperatures will have higher porosity, reducing the tendency for pores to become isolated upon annealing, but a reduced YSZ fraction will provide more freedom for structural changes such as Ni coarsening and decreased Ni connectivity as suggested by Simwonis et al. [12].

Acknowledgements

The authors gratefully acknowledge the financial support from the National Science Foundation Ceramics program through Grant DMR-0907639. The FIB-SEM was accomplished at the Electron Microscopy Center for Materials Research at Argonne National Laboratory, a US Department of Energy Office of Science Laboratory operated under Contract No. DE-AC02-06CH11357 by UChicago Argonne, LLC. Graduate student Kyle Yakal-Kremksi and undergraduate students Zach Patterson and Danni Jin are acknowledged for their help with manual segmentation required for some images. The authors also thank Hsun-Yi Chen and Prof. Katsuyo Thornton at the University of Michigan for the tortuosity calculations.

References

[1] F.N. Cayan, M. Zhi, S.R. Pakalapati, I. Celik, N. Wu, R. Gemmen, J. Power Sources 185 (2008) 595–602.
[2] Y. Matsuzaki, I. Yasuda, Solid State Ionics 132 (2000) 261–269.
[3] J.W. Fergus, Int. J. Hydrogen Energy 32 (2007) 3664–3671.
[4] Y. Matsuzaki, I. Yasuda, Solid State Ionics 132 (2000) 271–278.
[5] Y.L. Liu, C. Jiao, Solid State Ionics 176 (2005) 435–442.
[6] Y.L. Liu, S. Primdahl, M. Mogensen, Solid State Ionics 161 (2003) 1–10.
[7] S.P. Simner, M.D. Anderson, M.H. Engelhard, J.W. Stevenson, Electrochem. Solid-State Lett. 9 (2006) A478–A481.
[8] D.A. Osinkin, B.L. Kuzin, N.M. Bogdanovich, Russ. J. Electrochem. 46 (2010) 41–48.
[9] T. Matsui, R. Kishida, J.-Y. Kim, H. Muroyama, K. Eguchi, J. Electrochem. Soc. 157 (2010) B776–B781.
[10] S.P. Jiang, J. Mater. Sci. 38 (2003) 3775–3782.
[11] S.P. Jiang, W. Wang, Solid State Ionics 176 (2005) 1185–1191.
[12] D. Simwonis, F. Tietz, D. Stover, Solid State Ionics 132 (2000) 241–251.
[13] A. Faes, A. Hessler-Wyser, D. Presvytes, C.G. Vayenas, J. Van Herle, Fuel Cells 9 (2009) 841–851.
[14] P. Tanasini, M. Cannarozzo, P. Costamagna, A. Faes, J. Van Herle, A. Hessler-Wyser, C. Comninellis, Fuel Cells 9 (2009) 740–752.
[15] J.R. Wilson, J.S. Cronin, A.T. Duong, S. Rukes, H.-Y. Chen, K. Thornton, D.R. Mumm, S. Barnett, J. Power Sources 195 (2009) 1829–1840.
[16] T. Iwata, J. Electrochem. Soc. 143 (1996) 1521–1525.
[17] A. Hagen, R. Barfod, P.V. Hendriksen, Y.-L. Liu, S. Ramousse, J. Electrochem. Soc. 153 (2006) A1165–A1171.
[18] J.R. Wilson, W. Kobsiriphat, R. Mendoza, H.-Y. Chen, J.M. Hiller, D.J. Miller, K. Thornton, P.W. Voorhees, S.B. Adler, S.A. Barnett, Nat. Mater. 5 (2006) 541–544.
[19] J.R. Wilson, J.S. Cronin, S.A. Barnett, Scripta Mater. (2010), doi:10.1016/j.scriptamat.2010.09.025.
[20] P.R. Shearing, Q. Cai, J.I. Golbert, V. Yufit, C.S. Adjiman, N.P. Brandon, J. Power Sources 195 (2010) 4804–4810.
[21] H. Iwai, N. Shikazono, T. Matsui, H. Teshima, M. Kishimoto, R. Kishida, D. Hayashi, K. Matsuzaki, D. Kanno, M. Saito, H. Muroyama, K. Eguchi, N. Kasagi, H. Yoshida, J. Power Sources 195 (2009) 955–961.
[22] P.S. Jørgensen, K.V. Hansen, R. Larsen, J.R. Bowen, Ultramicroscopy 110 (2010) 216–228.
[23] D. Gostovic, J.R. Smith, D.P. Kundinger, K.S. Jones, E.D. Wachsman, Electrochem. Solid-State Lett. 10 (2007) B214–B217.
[24] H.-Y. Chen, H.-C. Yu, J.S. Cronin, J.R. Wilson, S.A. Barnett, K. Thornton, J. Power Sources 196 (2011) 1333–1337.
[25] J.R. Wilson, S.A. Barnett, Electrochem. Solid-State Lett. 11 (2008) B181–B185.
[26] J.D. Nicholas, S.A. Barnett, J. Electrochem. Soc. 157 (2010) B536–B541.
[27] J.R. Wilson, A.T. Duong, M. Gameiro, H.-Y. Chen, K. Thornton, D.R. Mumm, S.A. Barnett, Electrochem. Commun. 11 (2009) 1052–1056.
[28] J.R. Wilson, M. Gameiro, K. Mischaikow, W. Kalies, P.W. Voorhees, S.A. Barnett, Microsc. Microanal. 15 (2009) 71–77.
[29] L. Holzer, F. Indutnyi, P.H. Gasser, B. Münch, M. Wegmann, J. Microsc. 216 (2004) 84–95.
[30] J.R. Wilson, Ph.D. Thesis, Department of Materials Science and Engineering, Northwestern University, Evanston, IL, 2008, pp. 1–298.
[31] J. Wilson, J.S. Cronin, S. Rukes, A. Duong, D. Mumm, S.A. Barnett, ECS Trans. 25 (2009) 2283–2292.
[32] A. Leonide, V. Sonn, A. Weber, E. Ivers-Tiffee, J. Electrochem. Soc. 155 (2008) B36–B41.
[33] R. Barfod, M. Mogensen, T. Klemenso, A. Hagen, Y.-L. Liu, P.V. Hendriksen, J. Electrochem. Soc. 154 (2007) B371–B378.